ACS APPLIED MATERIALS & INTERFACES

Research Article

www.acsami.org

Modification of Properties of Yttria Stabilized Zirconia Epitaxial Thin Films by Excimer Laser Annealing

R. Bayati,*[,†] R. Molaei,[‡] A. Richmond,[§] S. Nori,[∥] F. Wu,[⊥] D. Kumar,[#] J. Narayan,*[,∥] J. G. Reynolds,[⊗] and C.L. Reynolds, Jr.[∥]

[†]Intel Corporation, IMO-RA, Hillsboro, Oregon 97124, United States

[‡]Intel Corporation, D1C, Hillsboro, Oregon 97124, United States

[§]Department of Materials Science and Engineering, University of Florida, Gainesville, Florida 32611, United States

[∥]Department of Materials Science and Engineering, North Carolina State University, EB-1, Raleigh, North Carolina 27695-7907, United States

[⊥]Princeton Institute for the Science and Technology of Materials (PRISM), Princeton University, Princeton, New Jersey 08540, United States

[#]Mechanical Engineering Department, North Carolina A&T State University, Greensboro, North Carolina 27411, United States

[⊗]Department of Physics, North Carolina State University, Raleigh, North Carolina 27695, United States

ABSTRACT: This study focuses on the ultrafast improvement of surface wettability, electrical, and room temperature magnetic characteristics of cubic zirconia single crystalline thin films after laser annealing. The point defects generated by the laser treatment are envisaged to play a critical role in altering the above properties. Yttria stabilized zirconia (YSZ) thin films were epitaxially grown on Si(100) substrates by pulsed laser deposition technique and subsequently annealed by a KrF excimer laser beam (τ = 25 ns) using low-energy laser pulses. An atomically sharp interface, parallel to the film free surface, between laser annealed layer and the pristine region was observed. The single crystalline nature of thin films was preserved following the laser treatment. The laser−solid interaction with YSZ led to the introduction of point defects, i.e., oxygen vacancies, resulting in a strained structure which, in turn, resulted in the formation of a tetragonal-like zirconia. With the increase of number of laser pulses the laser treated films got highly disordered due to the high concentration of the point defects, while maintaining their crystalline nature. Although the surface of the pristine sample showed weak hydrophilic characteristics (contact angle ∼ 73°), the laser annealed samples exhibited significantly improved hydrophilic characteristics. It was found that there is an optimum number of laser pulses where the maximum hydrophilicity (contact angle ∼ 22°) is obtained. The carrier concentration in the sample with the highest hydrophilicity was determined to be higher by about 5 orders of magnitude compared to the pristine sample. This sample possessed the lowest electrical resistivity. The laser annealed YSZ epilayers showed a superior room-temperature ferromagnetic behavior, compared to the pristine samples. A 2-fold enhancement in the magnetization of the samples was observed following the laser treatment which is a clear demonstration of the key role of defects and their transient distribution throughout the lattice. All these observations were correlated with the formation of point defects due to the photon interaction with YSZ and absorption of energy of the KrF laser photons to produce defects.

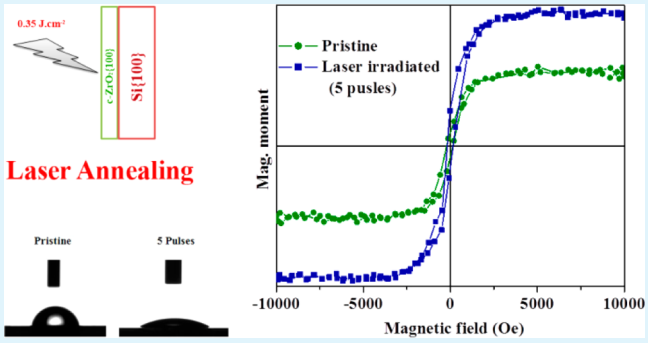

KEYWORDS: *ZrO_2, zirconia, epitaxy, wettability, conductivity, ferromagnetism, defect*

1. INTRODUCTION

Zirconium dioxide, also known as zirconia (ZrO_2), is a material of utmost importance, that is widely used in various applications including: catalysis,[1,2] catalyst supports,[3,4] dielectric materials,[5,6] high-performance ceramic materials,[7,8] chemical sensors,[9,10] solid oxide fuel cells,[11−13] thermal barrier coatings, and biomedical implants.[14−16] It exhibits an *n*-type electrical conductivity[17,18] that originates from the existence of oxygen vacancy and zirconium interstitial defects. Because zirconium interstitial defects require a high formation energy compared to all other defects,[19,20] it can be assumed that only oxygen vacancies are responsible for the *n*-type conductivity. The formation of other point defects, including zirconium antisite, zirconium vacancy, oxygen interstitial, oxygen antisite, results in

Received: September 15, 2014
Accepted: November 24, 2014
Published: December 4, 2014

a *p*-type electrical conductivity.[19] The lattice defects usually introduce localized energy levels within the band gap, which result in the energy emissions other than band-to-band transitions. This phenomenon leads to a smaller effective band gap if the density of energy levels is very high near the band edges.[21,22]

Pure zirconia (ZrO_2) crystallizes in three different polymorphs: monoclinic, tetragonal, and cubic. Its monoclinic structure is the thermodynamically stable state at room temperatures (T < 1170 °C). Monoclinic zirconia transforms to tetragonal and cubic zirconia at temperatures above 1170 and 2370 °C, respectively. Of course, the tetragonal and cubic phases of zirconia, which are of practical importance, can be stabilized at room temperature via doping with other oxides. Different oxides, such as yttrium oxide (Y_2O_3), calcium oxide (CaO), or magnesium oxide (MgO), can be added to zirconia as a stabilizer. For instance, the tetragonal state can be stabilized at room temperature by doping with 3 to 5 mol % of yttria. Lattice parameters of tetragonal yttria-stabilized zirconia, which belongs to the $P4_2/nmc$ space group, are a = 3.6067 Å and c = 5.1758 Å (for a 3 mol % yttria-doped ZrO_2). Yttria content of 8 mol % or higher leads to the cubic phase of zirconia stable at room temperature. Cubic yttria-stabilized zirconia has a fluorite-type structure with the space group $Fm\bar{3}m$. Its lattice parameter is 5.1289 Å (for a 15 mol % yttria-doped ZrO_2).[18,23] The thermal expansion coefficient of yttria-stabilized zirconia (called YSZ hereafter) is about 11.4×10^{-6} K^{-1}. YSZ has a high dielectric constant of 25 and a large band gap of 7.8 eV.[24,25] The values reported for the band gap energy (Eg) of YSZ range from 4.23 to 4.86 (YSZ) eV.[26−33] The relatively wide band gap along with the high negative value of the conduction band potential makes this material a catalyst for the production of hydrogen through splitting of water molecules.[26,27]

Recently, thin films of metal oxides have gained acceptance for advanced devices, such as zirconium and vanadium oxides[34] and compound oxides such as LSMO,[35] CGO,[36] and LSMCO[37] in fuel cells, titanium dioxide for photocatalysis,[38] tantalum and titanium oxide in random access memories,[39] zinc oxide in super capacitors,[40] zirconium oxide in radioactive waste disposal,[41] and nickel oxide in photochemical devices.[42] The efficiency and performance of thin film heterostructures are governed by materials science related aspects including microstructure, defect content, and size. In particular, many of the properties of a given material are dictated by the nature of defects and can be altered via manipulation of its defect content. To obtain desired properties, it is extremely important to introduce stable defects into the crystalline lattice in a controlled manner.

In this study, we have grown epitaxially cubic yttria-stabilized zirconia (c-YSZ) thin films on a Si(100) substrate. Then, defects are subsequently introduced in a controlled manner through laser annealing with nanosecond laser pulses at lower energies. This is a simple and fast technique influencing a thin surface layer whose thickness can be controlled by the energy of the laser pulse. We show that crystalline lattice structure and epitaxy are preserved after laser treatment, but there is a significant disorder in the oxygen lattice. It is further demonstrated that the hydrophobicity characteristics of the thin films can be changed from hydrophobic to hydrophilic by laser annealing. Electrical conductivity and concentration of charge carriers are significantly increased as well. We suggest that these observations can be attributed to point defects, which are formed due to the coupling of high energy laser photons with the YSZ surface. Thus, controlled modification of surface properties and electrical conductivity by introduction of defects stand impact profoundly catalysis, solid state ionics, and fuel cells.

2. EXPERIMENTAL SECTION

2.1. Thin Film Deposition and Laser Annealing. We employed a pulsed laser deposition (PLD) technique to grow epitaxial yttria-stabilized cubic zirconia (c-YSZ) thin films on Si(100) substrates. In our previous works,[42−44] we showed that zirconia can effectively destroy and remove the native oxide (SiO_x) layer from the surface of silicon substrates. As a consequence, epitaxial zirconia is able to grow directly on silicon and without the need for any buffer layer in between the substrate and the c-YSZ thin film. The Si(100) substrates were cleaned via a multistep process including degreasing in hot acetone for 5 min, ultrasonic cleaning in acetone for 5 min, and ultrasonic cleaning in methanol for 5 min at room temperature. Then, they were etched in dilute hydrogen fluoride (HF) solution for 30 s at room temperature. Immediately, these substrates were loaded into the PLD chamber. HF etching removes the oxide layer from the surface of the substrates and forms a hydrogen terminated surface, which prevents further oxidation of the surface before the deposition chamber. The chamber was evacuated to a background pressure of about 8×10^{-7} Torr. A yttria-stabilized ZrO_2 (8−10 mol % yttria) target was used as the sputtering source. A Lambda Physik (LPX200) KrF excimer laser (λ = 248 nm, τ = 25 ns) was employed to ablate the YSZ target as well as perform laser annealing at lower energy densities. The laser energy density and repetition rate were set at 3.0−3.5 J/cm^2 and 10 Hz. The YSZ thin films were deposited at 600 °C under an oxygen partial pressure of 5×10^{-4} Torr using 2000 pulses.

The samples were laser annealed subsequently for 1, 5, 10, and 15 pulses using the KrF excimer laser at an energy density of about 0.35 J·cm^{-2}. The dimensions of the laser affected region on the surface were measured to be about 6 × 10 mm.

2.2. Characterization. A Rigaku diffractometer equipped with a copper X-ray tube (Kα radiation, λ_{ave} = 0.154 nm) was used to collect both regular and high resolution θ-2θ patterns. A Philips X'Pert Pro X-ray diffractometer was also employed to collect φ patterns. Cross section transmission electron microscope (TEM) images and corresponding selected area electron diffraction (SAED) patterns were obtained using a JEOL 2010F transmission electron microscope equipped with a Gatan image filter (GIF). This microscope has a point-to-point resolution of 0.18 nm, while operating at 200 kV. Raman measurements were performed on both pristine and laser annealed films using a Renishaw Ramiscope. Spectra were recorded at room temperature in the z(-,-)-z backscattering configuration using a 514.5 nm excitation line of an Ar^+ laser at 20 mW output power. The system was calibrated using the 520.6 cm^{-1} Raman shift of Si, and the accuracy of the spectra was estimated to be ±1.5 cm^{-1}. An SPECS X-ray photoelectron spectrometer with a Mg Kα source (λ = 1254 eV) and a PHOIBIS 150 hemispherical analyzer were used to assess the surface stoichiometry of the films before and after the laser treatment. These results were interpreted using Version 4.1 SDP software.

2.3. Electrical Properties and Hall Measurement. The effect of laser annealing on the concentration of charge carriers and electrical conductivity was studied by Hall measurements where the measurements were performed at room temperature under a magnetic field of 0.55 T (5500 G). The Ohmic contacts to the YSZ thin films were made using gold wires attached to the films by freshly cleaved indium pads where the pads were arranged in a square geometry. The distance between the pads was about 5 mm. The temperature and humidity were controlled at about 70 and 50% during the electrical measurements, respectively.

2.4. Wettability. Hydrophobicity of the pristine and laser annealed YSZ surfaces under ambient conditions was monitored using a Rame-Hart Model 200 contact angle goniometer with deionized (DI) water as the liquid at room temperature. Special care was taken to keep a dust-free environment with low humidity.

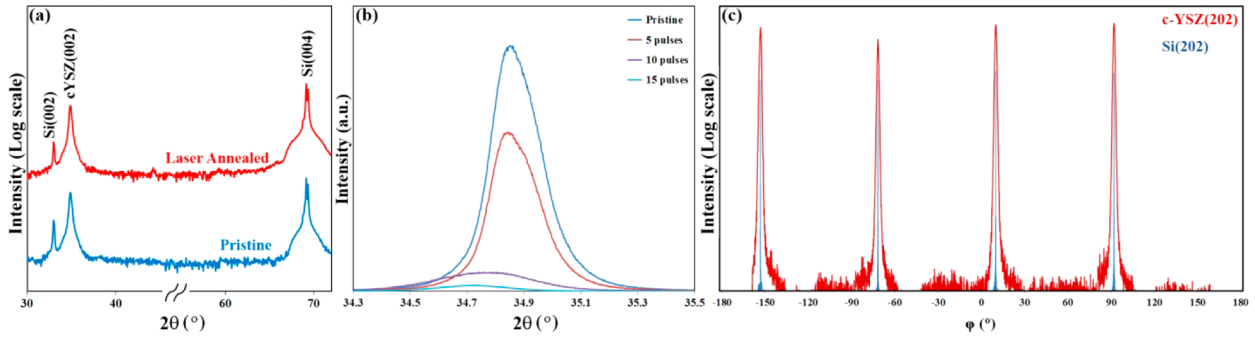

Figure 1. (a) XRD θ-2θ patterns collected from the pristine and the sample annealed for 5 pulses, (b) high resolution scans through c-YSZ{002} peak for the sample laser treated for several number of pulses, and (c) φ patterns taken from c-YSZ{202} and Si{202} reflections.

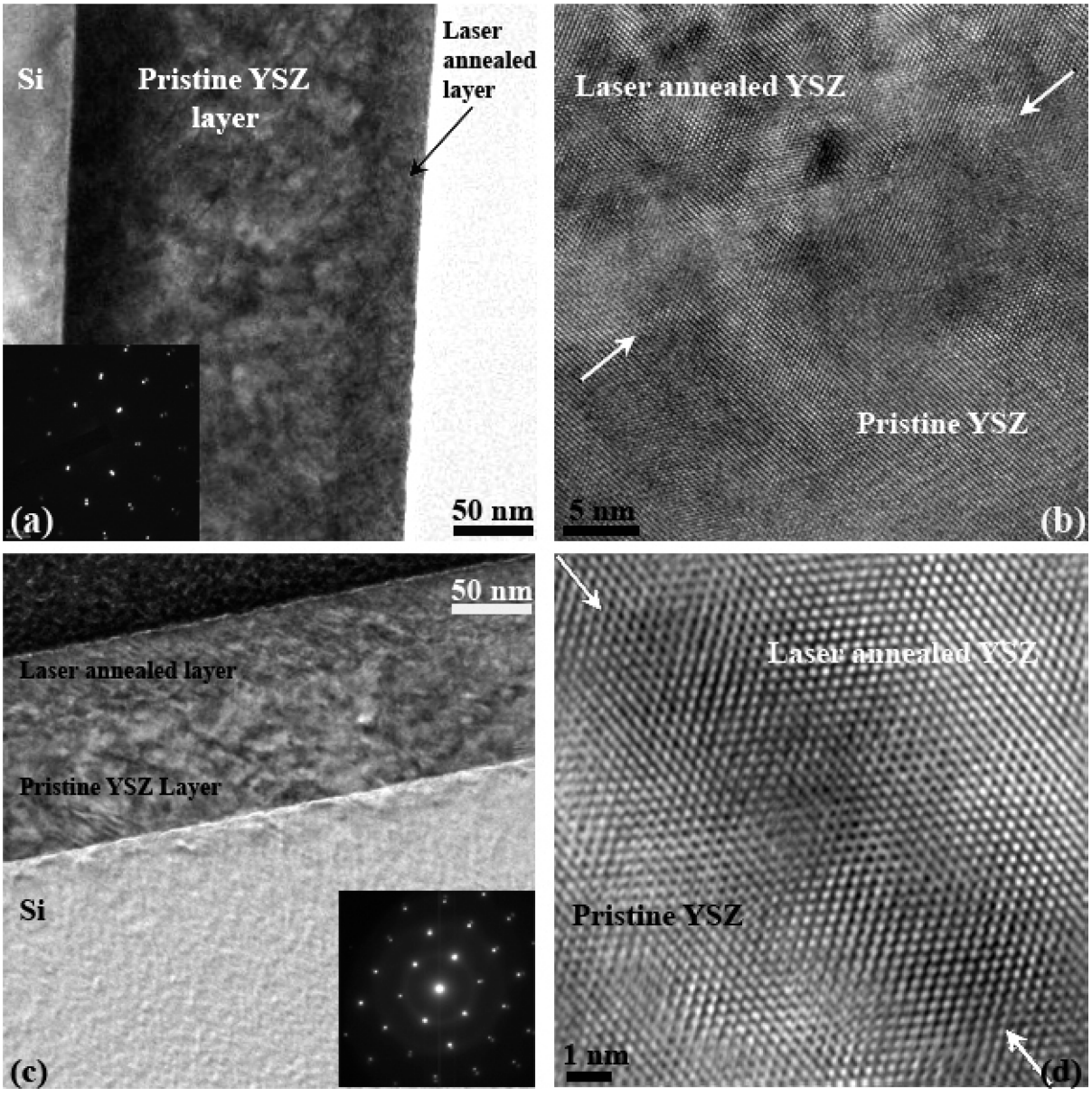

Figure 2. (a) Cross section TEM micrograph acquired from the sample annealed for 5 pulses. The corresponding SAED patterns, belonging to c-YSZ{110} and Si{110} zones, is shown in the inset. (b) High resolution image from the interface between pristine and laser annealed layers. The interface is shown by arrows. (c) Cross section image from the sample annealed for 15 pulses. The corresponding SAED pattern (from the c-YSZ{110} and Si{110} zones) is presented in the inset. (d) High resolution image from the interface between the pristine and the laser treated regions in the sample annealed for 15 pulses. The results clearly show that the crystalline nature has been preserved following laser treatment and no amorphous region has formed.

2.5. Magnetic Properties. Magnetic-field dependent magnetization (M-H) measurements were carried out using a physical property measurement system (PPMS) in conjunction with an Evercool-2 vibrating sample magnetometer (VSM) attachment (Quantum Design). For magnetization measurements, rectangular sample strips of 3 × 5 mm were used. Hysteresis measurements were performed by scanning the magnetic field from −10 to +10 kOe. The magnetic field was applied parallel to the film plane and great care was exercised not to contaminate the samples by handling them with clean nonmagnetic plastic tweezers during the entire measurement cycle.

3. RESULTS AND DISCUSSION

The θ-2θ X-ray diffraction patterns of the pristine and the 5-pulse laser annealed c-YSZ thin films are shown in Figure 1a. Both samples have the same out-of-plane orientations of ⟨100⟩. No new out-of-plane orientations are observed after the laser treatment. However, a shoulder is observed on the right-hand side of the c-YSZ{002} reflection in the high resolution X-ray patterns of the laser annealed samples, depicted in Figure 1b. These patterns belong to those from a pristine sample and samples that were laser treated by 5, 10, and 15 laser pulses. The reason why a shoulder is seen besides the main peak is that there are actually two distinct regions in the films contributing in the diffraction, i.e., laser treated region at the surface and an underlying portion of the pristine film that is not affected by the laser beam. These two regions exist after laser annealing that are associated with the absorption depth of the laser beam. The presence of these two different regions will be corroborated by cross section TEM micrographs (Figure 2). The laser annealed layer has different interplanar spacings due to the formation of point defects. Thus, there are actually two separate θ-2θ signals, originating from the pristine and the annealed regions, which merge with each other to form a single peak on the high resolution XRD patterns. Three features are worth noticing in Figure 1b. First, the full width at half-maximum (FWHM) of the c-YSZ{002} peak increases with number of laser pulses due to the strain in the lattice originating from the formation of point defects. Second, the peak intensity decreases significantly, as the number of pulse increases. The reason behind this observation is that the point defects decrease the structure factor of the planes and, hence, the XRD signal intensities. Third, a small Bragg peak shift toward lower 2θ values is observed in the laser treated samples. This shows that there is a tensile strain normal to the film surface, and the compressive strain in the film plane is corroborated from the Raman measurements shown in Figure 3. The strain along the normal direction to the surface in the samples laser annealed for 5, 10, and 15 pulses were calculated to be 0.01, 0.13, and 0.40%, respectively. These observations are attributed to the formation of lattice point defects due to the interaction of a high-power energy laser beam with the material.[43−46] The formation of point defects leads to a residual strain in the crystallographic lattice altering the interplanar spacing which, in turn, results in the XRD peak shift. The results indicate that a highly disordered regions form after 10 and 15 laser pulses. Our HRTEM studies (Figure 2) imply that no amorphous phase is formed and the overall crystalline structure of the laser annealed region is preserved. This point will be discussed in more detail later.

Figure 1c displays φ patterns from the c-YSZ thin film and Si substrate in the sample laser annealed for 5 pulses. Both patterns were collected from the {202} family of planes. The crystallographic parameters used to collect these patterns are summarized in Table 1. The appearance of four strong and sharp peaks from the c-YSZ thin film confirms a cube-on-cube epitaxial growth. As is seen, the peaks from c-YSZ and Si crystals have 90° azimuthal distances and appear at the same φ angles. Considering both θ-2θ and φ patterns as well as the 4-fold symmetry of these two crystals, a cube-on-cube growth with the epitaxial alignment between c-YSZ thin film and Si(100) substrate as $\langle 100\rangle\{100\}_{\text{c-YSZ}}\|\langle 100\rangle\{100\}_{\text{Si}}$ is established.

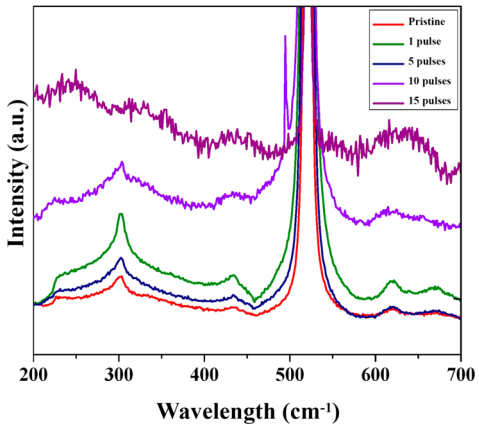

Figure 3. Raman spectra for pristine and laser annealed c-YSZ epilayers grown on Si(100) substrates.

Table 1. 2θ and ψ Angles Used to Acquire φ Patterns from c-YSZ{202} and Si{202} Reflections

reflection	2θ (deg)	Ψ (deg)
Si{202}	47.57	45
c-YSZ{202}	50.37	45

A cross section TEM micrograph taken from the sample laser annealed with 5 pulses and the corresponding SAED pattern are depicted in Figure 2a. The interface between annealed and pristine regions is flat and parallel to the free surface. The reason behind this observation is the short thermal diffusion distances and the large dimensions of the laser beam compared to the melt depth which limits the thermal gradients parallel to the interface to many orders of magnitude less than the gradients present perpendicular to the interface; as a consequence, heat flows essentially along a single direction normal to the surface.[43,47] The SAED pattern shown in the inset belongs to Si⟨110⟩ and c-YSZ⟨110⟩ zones. All spots on this pattern originate from these two zones, revealing that the initial structure of the c-YSZ thin film did not change following laser annealing with 5 pulses and the epitaxial relationship of the film to the substrate was maintained. The high resolution image in Figure 2b was acquired from the interface between pristine and the laser annealed layers. The interface has been underlined by arrows. It is clearly observed that the laser treated region has a crystalline structure. Figure 2c shows a low magnification cross section micrograph and the corresponding SAED pattern from the sample laser annealed for 15 pulses. A high resolution image from the interface between the laser affected region and the pristine region is depicted in Figure 2d. Both images ascertain that the crystalline nature has been maintained even after laser annealing by 15 pulses. An atomically sharp interface is observed between the pristine and the laser annealed layers. There are two possible reasons: (1) the surface did not melt at all, and (2) the surface melted, solidified, and the crystalline structure was maintained due to

Table 2. Summary of Raman Data for Pristine and Laser Annealed c-YSZ Thin Films

Raman mode	reference (cm^{-1}) [see ref 48]	pristine (cm^{-1})	1 pulse (cm^{-1})	5 pulses (cm^{-1})	10 pulses (cm^{-1})	15 pulses (cm^{-1})
Si	520.659	520.659	521.84	520.659	520.659	520.659
E_g stretch	256.4	225	227.47	225	213.94	not observed[a]
B_{1g} coupled bend and stretch	318.2	297.22	299.66	299.66	293.56	not observed[a]
E_g coupled bend and stretch	460.7	421.73	425.33	422.93	418.13	not observed[a]
A_{1g} symmetric stretch	603.4					
cubic F_{2g} symmetric stretch	617.2	614.88	613.68	611.335	604.31	not observed[a]
E_g asymmetric stretch	640	659.19	658.03	656.86	not observed[a]	not observed[a]

[a]Unable to discern due to high signal background.

the templating effect of the underlying pristine region. Of course, we will show later that the wettability, electrical, and magnetic properties of the annealed samples change as a function of number of pulses, further confirming that all experiments were conducted in solid-state regime and melting did not happen. In the solid state regime, the properties change as a function of number of pulses; in contrast, in the melt regime, the first pulse makes all changes and no further change is observed after the subsequent pulses.

Figure 3 shows the Raman spectra for the pristine film and for the films that were laser annealed for 1, 5, 10, and 15 pulses. In the pristine film, Raman shifts were observed at 225.0, 297.2, 421.7, 614.9, and 659.2 cm^{-1}, indicating the presence of both c-YSZ and tetragonal YSZ (t-YSZ). The t-YSZ phase is actually the t″ YSZ phase. This has been noted previously.[48−50] The appearance of more Raman active modes in the tetragonal form is related to its lower symmetry. Of course, the intensity of Raman peaks from tetragonal YSZ is far smaller than that of c-YSZ. The crystallographic structure of YSZ remarkably depends on the concentration of the stabilizer agent (yttria, herein), so even small deviations in the yttria content might result in the formation of tetragonal YSZ. These deviations might occur during the sputtering of the c-YSZ target during the film deposition. There are no diffraction spots from the tetragonal YSZ in the SAED pattern shown in Figure 2a, indicating t-ysz fraction to be small. In our previous works,[42,51] we showed that the tetragonal YSZ rotates by 45° when integrated epitaxially with Si{100} substrates. As is seen in Figure 1c, there is no φ-peak from YSZ at angular distances of 45° from those of silicon. Note that the patterns in Figure 1c are plotted in a log-scale where even tiny peaks can be easily seen. In addition, the Bragg peak from tetragonal YSZ(002) planes appears at 2θ of about 33.995°, which is not seen on the patterns shown in Figure 1a. We wish to emphasize that the initial content of the tetragonal YSZ is negligible compared to the c-YSZ and the tetragonal YSZ formed locally in the regions where there are some deviations in the yttria concentration. Of course, we will discuss that a pseudotetragonal YSZ forms following the laser treatment. Comparing our Raman shifts to those of stress-free YSZ compiled by Heiroth, et al.,[48] we note that our films are under tension, the magnitude of which is relatively constant for the pristine sample and those samples annealed for up to 5 laser pulses. Beyond this, however, the laser annealed portion of the film becomes more tensile as evidenced by the increased tensile shift in the cubic F_{2g} frequency. This is consistent with the high resolution XRD patterns (Figure 1b) where a peak shift toward lower 2θ's was observed as the number of laser pulses increased. The shift toward smaller 2θ values confirms a tensile strain along the out-of-plane direction. In addition, the large background observed in samples laser annealed for 10 and 15 pulses indicate that the laser annealed regions have been disordered, which is consistent with low intensity and large FWHM of the X-ray signals from these two samples shown in Figure 1b.

A summary of the relevant Raman peaks is given in Table 2. For the laser treated samples, we note that immediately beneath the laser annealed region, which was measured to be ∼43 nm after 5 laser pulses, a portion of the grown film which remains unannealed exists (pristine region). There are several observations that one can make from the Raman spectra in Figure 3 with regard to the frequency shifts and relative intensities of the observed Raman modes. First, the presence of clear Raman peaks indicate that our pristine and laser annealed films are crystalline. This observation is consistent with the X-ray spectra in Figure 1. The X-ray spectra also show a specific epitaxial orientational relationship of the YSZ film to the Si substrate. Second, the negative shifts in the E_g stretch and B_{1g} and E_g coupled bend and stretch tetragonal modes as well as the cubic F_{2g} symmetric stretch relative to their stress-free signatures indicate that the films are under tension. For all samples investigated, the Si Raman peak from the substrate is constant at 520.6 cm^{-1}, as expected, which confirms that the observed YSZ Raman shifts compared to the reference strain-free data are real. Also, within the uncertainty of the data, the magnitude of the shift is relatively independent of whether the sample is pristine or laser annealed after 1 or 5 pulses. However, as Table 2 reveals that the strain in the c-YSZ films becomes more tensile as the number of laser anneal pulses is increased beyond 5 pulses. For the spectra shown in Figure 3, we have intentionally offset via background subtraction the signal intensity for samples that were laser annealed for 10 and 15 pulses relative to the pristine and 1 and 5 pulse laser annealed samples to amplify that those measurements had high backgrounds resulting in a poor resolution of the high symmetry cubic stretch mode at 617.2 cm^{-1} as well as the other Raman active modes. The structural disorder from laser annealing with 10 pulses leads to a wider than expected fwhm of the F_{2g} mode. Further laser annealing with 15 pulses creates additional disorder such that the frequency shift of the tetragonal modes as well as cubic mode are difficult to discern due to the high signal background. As is seen in Figure 3, the Raman shifts from tetragonal YSZ become more intense in the laser annealed samples which is attributed to the formation of point defects and strain along the out-plane-orientation, as discussed earlier. The laser annealed layer is confined along the in-plane directions by the pristine layer; however, the unit cell can freely shrink or expand along the out-of-plane orientation. Hence, the in-plane dimensions of the YSZ unit cell cannot change following the incorporation of the point defects, whereas its out-of-plane dimensions does change; as a consequence, a pseudo tetragonal YSZ forms in the laser treated region. Laser-induced rapid heating and quenching

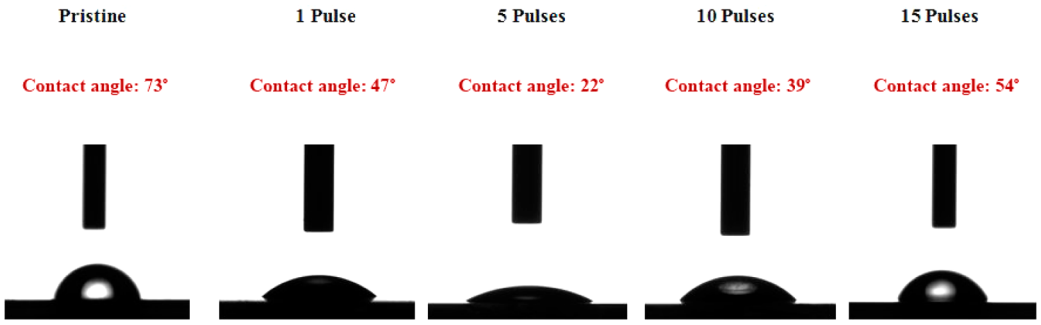

Figure 4. Effect of KrF laser annealing on surface wettability of c-YSZ{100} epilayers.

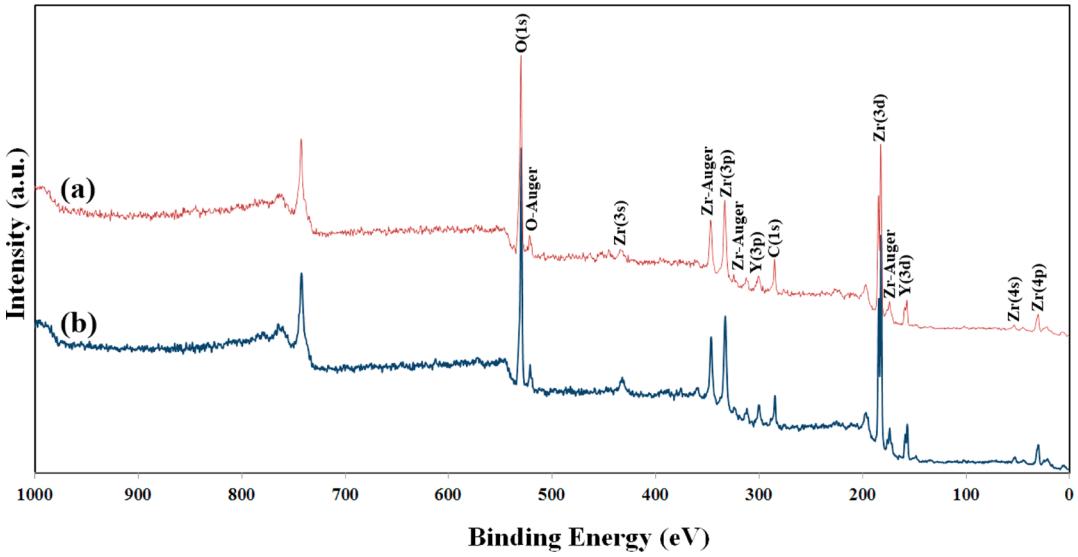

Figure 5. XPS survey scan acquired from the samples laser treated for: (a) 5 pulses and (b) 15 pulses.

seem to cause the formation of tetragonal phase. The pseudotetragonal YSZ is totally different from the t″ YSZ phase, as explained above.

Perhaps the most intriguing aspect of the Raman data relates to the spectra for 10 and 15 laser pulses. As we indicated above, the high background for the 10 and 15 laser pulses necessitated background subtraction; otherwise, it is difficult to discern the Raman peaks associated with the c-YSZ films such that essentially no c-YSZ peaks exist after laser annealing after 15 pulses. We attribute the large signal background observed in the 10 and 15 pulse samples to structural disorder in the laser annealed portion of the YSZ crystal. This assignment is also consistent with the X-ray data in Figure 1b, in which the YSZ(002) peak becomes significantly less intense and shifts to lower 2θ values, indicating increased strain in the films. Further examination of the mode assignments that have been reported in the literature (see, for example, Heiroth et al.[48] and Bouvier and Lucazeau[52]) provides additional insight on the impact of laser annealing. The E_g stretch (256 cm^{-1}) is attributed to displacements of O and Zr in the (x,y) plane whereas the B_{1g} (318 cm^{-1}) coupled bend and stretch mode involves O, Zr displacements along the z-direction.[46,48] The A_{1g} (603 cm^{-1}) symmetric and E_g asymmetric (640 cm^{-1}) stretches both involve O−Zr−O stretches. The mode (617 cm^{-1}) associated with the c-YSZ modification is also a symmetric O−Zr−O stretch. We should note that the E_g coupled bend and stretch at 461 cm^{-1}, which Heiroth, et al.[46] associated with a Zr−O bend and stretch mode, was attributed to O displacements along the z-direction only by Bouvier and Lucazeau.[52] It is this mode that exhibits the largest shift from the reference strain-free value. Because the mode assignments involve coupled displacements in both the O and Zr sublattices, one can, thus, conclude that the structural disorder observed in the Raman and X-ray diffraction data with 10 and 15 laser pulses is most likely associated with general disorder within the laser annealed region due to formation of a heavily defective YSZ.

Results of wettability measurements are shown in Figure 4. While the pristine sample exhibits an almost hydrophobic behavior with a contact angle of ∼73°, the laser annealed samples, for example the sample laser treated for 5 shots, become more hydrophilic with a contact angle ∼22°. The hydrophilicity behavior is suppressed in the samples annealed for 10 and 15 pulses where the contact angles were measured to be about 39 and 54°, respectively. The commonly accepted mechanism of hydrophilicity in oxide materials is based upon the generation of e^-−h^+ pairs at the conduction and valence bands which initiate various redox reactions at the surface. The photogenerated charge carriers are trapped by surface O^{2-} ions to create oxygen vacancies:

$$ZrO_2 + h\upsilon \rightarrow e' + h^{\bullet} \quad (1)$$

$$O_O'' + 2h^{\bullet} \rightarrow 1/2O_2 + V_O \quad (2)$$

The formation energy of oxygen vacancies in YSZ is negative under low oxygen pressure conditions and a few electron volts in oxygen-rich atmospheres; therefore, this defect can form very

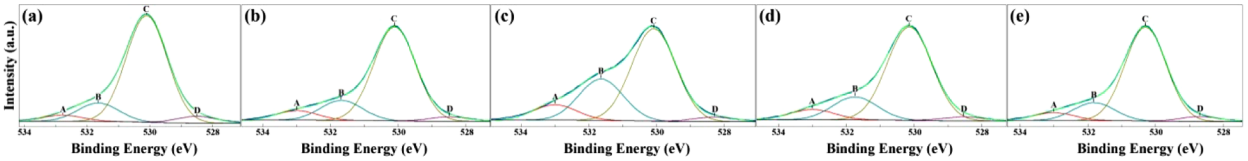

Figure 6. XPS O(1s) core level binding energy in YSZ{100} epilayers (a) Pristine sample and the samples laser treated for (b) 1 pulse, (c) 5 pulses, (d) 10 pulses, and (e) 15 pulses.

easily.[19] It is worth mentioning that the reported values for the band gap of YSZ are mainly below 5 eV,[23,25−33,53] so energy of KrF excimer laser photon (λ = 248 nm, Eg = ∼5 eV) can be absorbed by the electronic structure of YSZ. According to this model, water molecules are dissociatively adsorbed at the defect sites.[54,55] In other studies by our group, we demonstrated that the photochemical, electrical, magnetic, and optical properties of metal oxides can be systematically altered in a controlled manner by laser irradiation.[44,45,56] It was revealed that oxygen vacancies that are generated by laser treatments play a critical role in altering the properties of the material. Oxygen vacancies, as prerequisites for hydrophilicity, form via two mechanisms. First, energy of the laser photons is absorbed by zirconia via photoexcitation of the valence electrons to the conduction band giving rise to the formation of oxygen vacancies, as explained above. Second, temperature of the surface is raised due to the coupling of the high energy laser beam with the surface giving rise to the reduction of ZrO_2 and, thus, the formation of oxygen vacancies. In this case, laser-sold interactions cause rapid heating via transient transfer of energy from laser photons to phonons in times of the order of a picosecond.[57,58] Considering the energy density used for laser annealing (0.35 J·cm^{-2}), the actual surface temperature is time dependent and may increase over 1000 °C.[45] Following the formation of oxygen vacancies on the surface, water molecules adsorb on the defect sites dissociatively. As a result, a new hydroxyl group is produced, which is responsible for the highly hydrophilic surface. It should be noted that the laser energy, in all experiments, is below the melting threshold of YSZ and our experiments were performed in the solid-state regime where the surface morphology does not significantly change. Therefore, the surface morphology of all samples is almost similar and its effect on hydrophilicity can be neglected.

Figure 5 displays XPS survey spectra collected from the samples annealed for 5 and 15 samples. The patterns clearly show that the samples contained O, Zr, Y, and C elements.

The formation of oxygen vacancies due to laser annealing was confirmed by XPS. Figure 6 shows the O(1s) core level binding energy of c-YSZ epitaxial thin films that were laser annealed for varying number of shots. In all interpretations, the binding energy of C(1s) peak was set at 285.0 eV as a reference. The peak was deconvoluted into four distinct peaks. Peaks A and B with binding energies of about ∼532.9 and 531.7 eV represent oxygen in water and hydroxyl groups attached to defect sites at the surface. Water molecules and hydroxyl groups are almost always present on oxide free surfaces. The surface of metal oxides becomes hydrated when exposed to the atmosphere. Hydroxyl groups couple with surface oxygen vacancies and, then, water molecules interact with these groups by means of hydrogen bonds.[59] So, the concentration of surface oxygen vacancies can be indirectly estimated by the portion of peak B. Peak C, located at a binding energy of ∼530.1 eV is assigned to the oxygen in YSZ lattice; in other words, it represents the perfection of YSZ. Finally, peak D with a binding energy of about 528.2−528.6 eV is attributed to oxygen in nonstoichiometric zirconia. The results show that the portion of peak B initially increases, reaches a maximum in the sample annealed by five laser pulses, and then decreases. The portion of peak C shows a reverse behavior. Its portion was calculated to be about 73.5, 60.0, 71.5, and 75.5% in the samples annealed for 1, 5, 10, and 15 laser pulses. The portion of peak C was measured to be about 77.3% in the pristine sample. Taking the XPS results into consideration, it can be deduced that the sample annealed by 5 pulses possesses the highest defect concentration near the surface.

Results of electrical measurements are displayed in Figure 7 where all laser treated samples show higher carrier concentration and conductivity than the pristine sample. Being in complete agreement with wettability results, the sample annealed with 5 laser pulses shows the highest carrier concentration and the lowest resistivity. It is worth reminding this sample had the largest number of oxygen vacancies at the surface (Figure 6). Because the change in properties depends on the number of pulses, it is deduced that all experiments were done in the solid state regime; in other words, the energy of the laser photons were below the melting threshold of YSZ and, therefore, the surface of the samples was not melted following the laser treatment. In the liquid regime, only a single pulse is enough to make all the changes and the number of pulses does not influence the properties. All samples showed *n*-type electrical conductivity, i.e., negative Hall coefficients. It necessarily means that oxygen vacancies and zirconium interstitials are the dominant point defects in all the samples in this study. It has been already shown that oxygen vacancies and zirconium interstitials are the origin of *n*-type conductivity, while the formation of other point defects, including zirconium antisite, zirconium vacancy, oxygen interstitial, oxygen antisite, results in a *p*-type electrical conductivity.[19] Zirconium interstitial requires the creation of two oxygen vacancies and

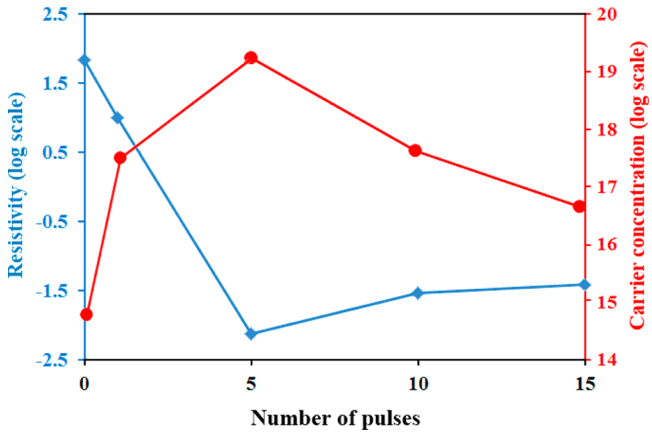

Figure 7. Effect of KrF laser annealing on electrical conductivity and charge carrier concentration in c-YSZ{100} epilayers.

displacing a zirconium cation from its original lattice site to an interstitial site. Generally speaking, zirconium interstitials have high formation energies compared with all other native defects[20] and their formation is unlikely. As a consequence, it can be deduced that oxygen vacancies are the dominant point defects in our samples.

Our results reveal that laser annealing increases the defect concentration in our YSZ thin films, leading to an enhanced hydrophilicity, carrier concentration, and electrical conductivity. This is the case when the number of laser pulses is less than an optimum value (5 shots); however, it adversely impacts these properties when the number of pulses increases beyond the optimum value. We attribute this observation to three factors. First, when the concentration of point defects increases beyond an optimum value, they act as scattering centers against charge carriers giving rise to a decreased electrical conductivity. Second, the energy level of point defects within the band gap of materials is affected by their concentration. The energy level of oxygen vacancies lies about 1 eV below the conduction band, so it can trap the excited electrons and enhance the charge separation which, in turn, improves the photochemical electrical properties. However, this energy level approaches the Fermi level at the middle of the band gap, when the concentration of oxygen vacancies increases. The electrons can no longer get trapped at these high defect contents. Meanwhile, under particular circumstances, both electrons and holes are trapped by the defects whose energy level resides at the middle of the band gap. Such defects act as charge recombination centers. In both cases, charge separation is suppressed. Third, the clustering of vacancy defects occurs in samples annealed for 10 and 15 pluses, which results in deactivating the defects. The clustered vacancies form vacancy loops lead to reduced carriers.

In addition, the laser treated samples exhibited room temperature ferromagnetism (RTFM). The isothermal field dependence of magnetic moment curves of pristine and laser annealed YSZ films deposited on Si(100) substrates measured at 300 K is plotted in Figure 8. The bottom inset of Figure 8 is the low-field M-H hysteresis loops between ±400 Oe clearly showing considerable coercivity of about 200 Oe. The diamagnetic contribution by silicon substrate has been subtracted. The important and interesting aspect of the above plot is that the saturation magnetization is enhanced significantly by more than 2-fold after laser irradiation treatment. The room temperature ferromagnetism and a significant increase in the saturation magnetization after the pristine sample has been subjected to laser irradiation (5 pulses) ought to have its origin in the formation of native point defects such as oxygen vacancies and other complexes, which are created by the high power laser pulses. The 2-fold enhancement in the magnetization of the samples is indeed a clear demonstration of the key role played by the defects and their mediation for three-dimensional ordering. In other words, oxygen vacancy creation and their dynamic distribution across the entire the lattice, result in the important changes in physical properties especially in electrical and magnetic properties in a significant way.

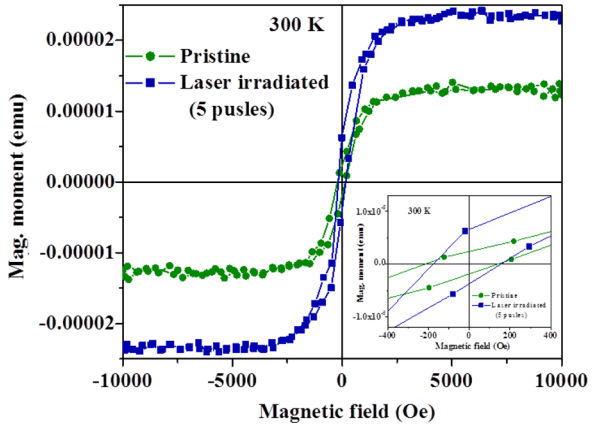

Figure 8. Isothermal field dependence of magnetic moment curves of pristine and laser annealed YSZ films deposited on Si(100) substrates measured at 300 K. The inset is the low-field M-H hysteresis loops between ±400 Oe clearly showing considerable coercivity ~200 Oe.

4. CONCLUSIONS

In summary, c-YSZ epitaxial thin films were grown on Si(100) substrates and subsequently annealed by nanosecond KrF excimer laser pulses. Our results showed that the single crystalline nature and both in-plane and out-of-plane orientations were preserved after the laser treatment. It was shown that a tetragonal-like YSZ formed due to the strain originating from the incorporation of point defects to the lattice. With the increase of number of laser pulses, the laser treated YSZ film became highly disordered; however, its crystalline nature was preserved and no amorphous phase formed. The interface between laser annealed and the pristine regions were atomically sharp, flat, and parallel to the surface. The pristine sample showed poor hydrophilic characteristics, while the laser annealed samples exhibited highly hydrophilic characteristics and the contact angle decreased from about 73° to about 22° following the laser annealing. It was found that there is an optimum number of shots where the maximum hydrophilicity is obtained. The carrier concentration in the sample with the highest hydrophilicity was higher than that in the pristine sample by about 5 orders of magnitude. This sample treated with 5 pulses exhibited the lowest electrical resistivity. An enhanced room temperature ferromagnetism (RTFM) was observed in the laser treated samples. All these observations were attributed to the formation of point defects due to the coupling of high energy laser beam with YSZ crystals.

AUTHOR INFORMATION

Corresponding Authors

*R. Bayati. E-mail: reza.bayati@intel.com, mbayati@ncsu.edu. Tel.: +1 (408) 204 2821. Fax: +1 (503) 613 8264.

*J. Narayan. E-mail: j_narayan@ncsu.edu. Tel.: 919-515-7874. Fax: 919-515-7724.

Notes

The authors declare no competing financial interest.

ACKNOWLEDGMENTS

We acknowledge NSF support through DMR-1304607 (JN-PI) and the REU site on Advanced Materials for Environmental Sustainability under grant EEC 1156762.

REFERENCES

(1) Poston, M. J.; Aleksandrov, A. B.; Sabo, D.E.; Zhang, Z. J.; Orlando, T. M. UV Photon-Induced Water Decomposition on Zirconia Nanoparticles. *J. Phys. Chem. C* **2014**, *118*, 12789−12795.

(2) Chorghade, R.; Battilocchio, C.; Hawkins, J. M.; Ley, S. V. Sustainable Flow Oppenauer Oxidation of Secondary Benzylic

Alcohols with a Heterogeneous Zirconia Catalyst. *Org. Lett.* **2013**, *15*, 5698−5701.
(3) Wang, S.; Yin, K.; Zhang, Y.; Liu, H. Glycerol Hydrogenolysis to Propylene Glycol and Ethylene Glycol on Zirconia Supported Noble Metal Catalysts. *ACS Catal.* **2013**, *3*, 2112−2121.
(4) Biasi, P.; Menegazzo, F.; Canu, P.; Pinna, F.; Salmi, T. O. Role of a Functionalized Polymer (K2621) and an Inorganic Material (Sulphated Zirconia) as Supports in Hydrogen Peroxide Direct Synthesis in a Continuous Reactor. *Ind. Eng. Chem. Res.* **2013**, *52*, 15472−15480.
(5) Gong, Y.; Zhai, H.; Liu, X.; Kong, J.; Wu, D.; Li, A. Impact of Gd_2O_3 Passivation Layer on Interfacial and Electrical Properties of Atomic-Layer-Deposited ZrO_2 Gate Dielectric on GaAs. *Appl. Surf. Sci.* **2014**, *291*, 35−39.
(6) Huang, J. J.; Huang, L. T.; Tsai, M. C.; Lee, M. H.; Chen, M. J. Enhancement of Electrical Characteristics and Reliability in Crystallized ZrO_2 Gate Dielectrics Treated with in-Situ Atomic Layer Doping of Nitrogen. *Appl. Surf. Sci.* **2014**, *305*, 214−220.
(7) Mazaheri, M.; Simchi, A.; Dourandish, M.; Golestani-Fard, F. Master Sintering Curves Of a Nanoscale 3Y-TZP Powder Compacts. *Ceram. Int.* **2009**, *35*, 547−554.
(8) Khattab, R. M.; Wahsh, M.M. S.; Khalil, N. M.; Gouraud, F.; Huger, M.; Chotard, T. Effect of Nanospinel Additions on the Sintering of Magnesia−Zirconia Ceramic Composites. *ACS Appl. Mater. Interfaces* **2014**, *6*, 3320−3324.
(9) Anggraini, S. A.; Breedon, M.; Ikeda, H.; Miura, N. Insight into the Aging Effect on Enhancement of Hydrogen-Sensing Characteristics of a Zirconia-based Sensor Utilizing a Zn−Ta−O-based Sensing Electrode. *ACS Appl. Mater. Interfaces* **2013**, *5*, 12099−12106.
(10) Ko, Y. S.; Kwon, Y. U. Mesoporous Zirconia Thin Films with Three-Dimensional Pore Structures and Their Application to Electrochemical Glucose Detection. *ACS Appl. Mater. Interfaces* **2013**, *5*, 3599−3606.
(11) Li, X.; Yu, Y.; Meng, Y. Novel Quaternized Poly(arylene ether sulfone)/Nano-ZrO_2 Composite Anion Exchange Membranes for Alkaline Fuel Cells. *ACS Appl. Mater. Interfaces* **2013**, *5*, 1414−1422.
(12) Mohammadi, G.; Jahanshahi, M.; Rahimpour, A. Fabrication and Evaluation of Nafion Nanocomposite Membrane Based on ZrO_2−TiO_2 Binary Nanoparticles as Fuel Cell MEA. *Int. J. Hydrogen Energy* **2013**, *38*, 9387−9394.
(13) Liu, Y.; Chen, J.; Wang, F.; Chi, B.; Pu, J.; Jian, L. Performance Stability of Impregnated $La_{0.6}Sr_{0.4}Co_{0.2}Fe_{0.8}O_{3-\delta}$−$Y_2O_3$ Stabilized ZrO_2 Cathodes of Intermediate Temperature Solid Oxide Fuel Cells. *Int. J. Hydrogen Energy* **2014**, *39*, 3404−3411.
(14) Yen, S. K.; Chiou, S. H.; Wu, S. J.; Chang, C. C.; Lin, S. P.; Lin, C. M. Characterization of Electrolytic HA/ZrO_2 Double Layers Coatings on Ti−6Al−4V Implant Alloy. *Mater. Sci. Eng., C* **2006**, *26*, 65−77.
(15) Samanipour, F.; Bayati, M. R.; Golestani-Fard, F.; Zargar, H. R.; Troczynski, T.; Mirhabibi, A. R. An Innovative Technique to Simply Fabricate ZrO_2−HA−TiO_2 Nanostructured Layers. *Colloid. Surf., B* **2011**, *86*, 14−20.
(16) Balla, V. K.; Xue, W.; Bose, S.; Bandyopadhyay, A. Laser-Assisted Zr/ZrO_2 Coating on Ti for Load-Bearing Implants. *Acta Biomater.* **2009**, *5*, 2800−2809.
(17) Neppolian, B.; Wang, Q.; Yamashita, H.; Choi, H. Synthesis and Characterization of ZrO_2−TiO_2 Binary Oxide Semiconductor Nanoparticles: Application and Interparticle Electron Transfer Process. *Appl. Catal., A* **2007**, *333*, 264−271.
(18) Nawale, A. B.; Kanhe, S. N.; Bhoraskar, S. V.; Mathe, V. L.; Das, A. K. Influence of Crystalline Phase and Defects in the ZrO_2 Nanoparticles Synthesized by Thermal Plasma Route on Its Photocatalytic Properties. *Mater. Res. Bull.* **2012**, *47*, 3432−3439.
(19) Liu, B.; Xiao, H.; Zhang, Y.; Aidhy, D. S.; Weber, W. J. Investigation of Oxygen Point Defects in Cubic ZrO_2 by Density Functional Theory. *Comput. Mater. Sci.* **2014**, *92*, 22−27.
(20) Youssef, M.; Yildiz, B. Intrinsic Point-Defect Equilibria in Tetragonal ZrO_2: Density Functional Theory Analysis with Finite-Temperature Effects. *Phys. Rev.* **2012**, *B86*, 144109−144114.
(21) Miyazaki, S. Characterization of High-k Gate Dielectric/Silicon Interfaces. *Appl. Surf. Sci.* **2002**, *190*, 66−74.
(22) Fang, D.; Luo, Z.; Liu, S.; Zeng, T.; Liu, L.; Xu, J.; Bai, Z.; Xu, W. Photoluminescence Properties and Photocatalytic Activities of Zirconia Nanotube Arrays Fabricated by Anodization. *Optic. Mater.* **2013**, *35*, 1461−1466.
(23) Ji, Z.; Rigsbee, J. M. Growth of Tetragonal Zirconia Coatings by Reactive Sputter Deposition. *J. Am. Ceram. Soc.* **2001**, *84*, 2841−2844.
(24) Kelly, J. R.; Denry, I. Stabilized Zirconia as a Structural Ceramic: An Overview. *Dent. Mater.* **2008**, *24*, 289−298.
(25) Hannink, R. H. J.; Kelly, P. M.; Muddle, B. C. Transformation Toughening in Zirconia-Containing Ceramics. *J. Am. Ceram. Soc.* **2000**, *83*, 461−487.
(26) Sayama, K.; Arakawa, H. Photocatalytic Decomposition of Water and Photocatalytic Reduction of Carbon Dioxide over Zirconia Catalyst. *J. Phys. Chem.* **1993**, *97*, 531−533.
(27) Botta, S. G.; Navıo, S. G.; Hidalgo, M. C.; Restrepo, G. M.; Litter, M. I. Photocatalytic Properties of ZrO_2 and Fe/ZrO_2 Semiconductors Prepared by a Sol−Gel Technique. *J. Photochem. Photobiol., A* **1999**, *129*, 89−99.
(28) Bendoraitis, J. G.; Salomon, R. E. Optical Energy Gaps in the Monoclinic Oxides of Hafnium and Zirconium and Their Solid Solutions. *J. Phys. Chem.* **1965**, *69*, 3666−3667.
(29) Newmark, A. R.; Stimming, U. Photoelectrochemical Studies of Passive Films on Zirconium and Amorphous Iron-Zirconium Alloys. *Langmuir* **1987**, *3*, 905−910.
(30) Preusser, S.; Stimming, U.; Wippermann, K. An Optical and Electrochemical Investigation of ZrO_2 Thin Films (from NM to MM thickness). *Electrochim. Acta* **1994**, *39*, 1273−1280.
(31) Sato, S.; Kadowaki, T. Photocatalytic Activities of Metal Oxide Semiconductors for Oxygen Isotope Exchange and Oxidation Reactions. *J. Catal.* **1987**, *106*, 295−300.
(32) Ganguly, K.; Sarkar, S.; Bhattacharyya, S. Zirconium Dioxide: A New Photosensitizer under UV Irradiation. *J. Chem. Soc., Chem. Comm.* **1993**, 682−683.
(33) PaiVerneker, V. R.; Petelin, A. N.; Crowne, F. J.; Nagle, D. C. Color-Center-Induced Band-Gap Shift in Yttria-Stabilized Zirconia. *Phys. Rev. B* **1989**, *40*, 8555−8557.
(34) Overmeere, Q. V.; Kerman, K.; Ramanathan, S. Energy Storage in Ultrathin Solid Oxide Fuel Cells. *Nano Lett.* **2012**, *12*, 3756−3760.
(35) Su, Q.; Yoon, D.; Sisman, Z.; Khatkhatay, F.; Jia, Q.; Manthiram, A.; Wang, H. Vertically Aligned Nanocomposite $La_{0.8}Sr_{0.2}MnO_{3-\delta}$/$Zr_{0.92}Y_{0.08}O_{1.96}$ Thin Films as Electrode/Electrolyte Interfacial Layer for Solid Oxide Reversible Fuel Cells. *Int. J. Hydrogen Energy* **2013**, *38*, 16320−16327.
(36) Constantin, G.; Rossignol, C.; Barnes, J.-P.; Djurado, E. Interface Stability of Thin, Dense CGO Film Coating on YSZ for Solid Oxide Fuel Cells. *Solid State Ionics* **2013**, *235*, 36−41.
(37) Chen, X.; Zhang, L.; Liu, E.; Jiang, S. P. A Fundamental Study Of Chromium Deposition and Poisoning at $(La_{0.8}Sr_{0.2})_{0.95}(Mn_{1-x}Co_x)$-$O_{3\pm\delta}$ ($0.0 \leq x \leq 1.0$) Cathodes of Solid Oxide Fuel Cells. *Int. J. Hydrogen Energy* **2011**, *36*, 805−821.
(38) Bayati, M. R.; Ding, J.; Lee, Y. F.; Narayan, R. J.; Narayan, J. Defect Mediated Photocatalytic Decomposition of 4-Chlorophenol on Epitaxial Rutile Thin Films Under Visible and UV Illuminations. *J. Phys.: Condens. Matter* **2012**, *24*, 395005.
(39) Yang, Y.; Choi, S. H.; Lu, W. Oxide Heterostructure Resistive Memory. *Nano Lett.* **2013**, *13*, 2908−2915.
(40) Han, H. C.; Chong, C. W.; Wang, S. B.; Heh, D.; Tseng, C. A.; Huang, Y. F.; Chattopadhyay, S.; Chen, K. H.; Lin, C. F.; Lee, J. H.; Chen, L. C. High *K* Nanophase Zinc Oxide on Biomimetic Silicon Nanotip Array as Supercapacitors. *Nano Lett.* **2013**, *13*, 1422−1428.
(41) Molaei, R.; Bayati, M. R.; Alipour, H. M.; Nori, S.; Narayan, J. Enhanced Photocatalytic Efficiency In Zirconia Buffered n-NiO/p-NiO Single Crystalline Heterostructures by Nanosecond Laser Treatment. *J. Appl. Phys.* **2013**, *113*, 233708.
(42) Bayati, M. R.; Alipour, H. M.; Joshi, S.; Molaei, R.; Narayan, R. J.; Narayan, J.; Misture, S. T. Thin film Epitaxy and Enhancement of Photocatalytic Activity of Anatase/Zirconia Heterostructures by

Nanosecond Excimer Laser Treatment. *J. Phys. Chem. C* **2013**, *117*, 7138−7147.
(43) Bayati, M. R.; Joshi, S.; Molaei, R.; Narayan, R. J.; Narayan, J. Ultrafast Switching in Wetting Properties of TiO_2/YSZ/Si(001) Heteroepitaxy Induced by Laser Irradiation. *J. Appl. Phys.* **2013**, *113*, 063706.
(44) Molaei, R.; Bayati, R.; Narayan, J. Crystallographic Characteristics and p-Type to n-Type Transition in Epitaxial NiO Thin Film. *Cryst. Growth Des.* **2013**, *13*, 5459−5465.
(45) Mal, S.; Nori, S.; Narayan, J.; Prater, J. T. Defect-Mediated Ferromagnetism and Controlled Switching Characteristics in ZnO. *J. Mater. Res.* **2011**, *26*, 1298−1308.
(46) Mal, S.; Narayan, J.; Nori, S.; Prater, J. T.; Kumar, D. Defect-Mediated Room Temperature Ferromagnetism in Zinc Oxide. *Solid State Commun.* **2010**, *150*, 1660−1664.
(47) Singh, R. K.; Narayan, J. A Novel Method for Simulating Laser-Solid Interactions in Semiconductors and Layered Structures. *Mater. Sci. Eng., B* **1989**, *3*, 217−230.
(48) Heiroth, S.; Frison, R.; Rupp, J. L. M.; Lippert, T.; Barthazy Meier, E. J.; Gubler, E. M.; Dobeli, M.; Conder, K.; Wokaun, A.; Gauckler, L. J. Crystallization and Grain Growth Characteristics of Yttria-Stablized Zirconia Thin Films Grown by Pulsed Laser Deposition. *Solid State Ionics* **2011**, *191*, 12−23.
(49) Yashima, M.; Ohtake, K.; Kakihana, M.; Arashi, H.; Yoshimura, M. Determination of Tetragonal-Cubic Phase Boundary of $Zr_{1-x}R_xO_{2-x/2}$ (R = Nd, Sm, Y, Er and Yb) by Raman Scattering. *J. Phys. Chem. Solids* **1996**, *57*, 17−24.
(50) Yashima, M.; Kakihana, M.; Yoshimura, M. Metastable-Stable Phase Diagrams in the Zirconia-Containing Systems Utilized in Solid-Oxide Fuel Cell Application. *Solid State Ionics* **1996**, *86*−*88*, 1131−1149.
(51) Aggarwal, R.; Zhou, H.; Jin, C.; Narayan, J.; Narayan, R. J. Semipolar R-Plane ZnO Films on Si(100) Substrates: Thin Film Epitaxy and Optical Properties. *J. Appl. Phys.* **2010**, *107*, 113530.
(52) Bouvier, P.; Lucazeau, G. Raman Spectra and Vibrational Analysis of Nanometric Tetragonal Zirconia under High Pressure. *J. Phys. Chem. Solids* **2000**, *61*, 569−578.
(53) Korkmaz, S.; Pat, S.; Ekem, N.; Balbağ, M. Z.; Temel, S. Thermal Treatment Effect on the Optical Properties of ZrO_2 Thin Films Deposited by Thermionic Vacuum Arc. *Vacuum* **2012**, *86*, 1930−1933.
(54) Sakai, N.; Fujishima, A.; Watanabe, T.; Hashimoto, K. Enhancement of the Photoinduced Hydrophilic Conversion Rate of TiO_2 Film Electrode Surfaces by Anodic Polarization. *J. Phys. Chem. B* **2001**, *105*, 3023−3026.
(55) Simonsen, M. E.; Li, Z.; Sogaard, E. G. Influence of the OH Groups on the Photocatalytic Activity and Photoinduced Hydrophilicity of Microwave Assisted Sol−Gel TiO_2 Film. *Appl. Surf. Sci.* **2009**, *255*, 8054−8062.
(56) Gupta, P.; Dutta, T.; Mal, S.; Narayan, J. Controlled p-Type to n-Type Conductivity Transformation in NiO Thin Films by Ultraviolet-Laser Irradiation. *J. Appl. Phys.* **2012**, *111*, 013706.
(57) Singh, R. K.; Holland, O. W.; J. Narayan, O. W. Theoretical Model for Deposition of Superconduciing Thin Films Using Pulsed Laser Evaporation Technique. *J. Appl. Phys.* **1990**, *68*, 233.
(58) Singh, R. K.; Narayan, J. Pulsed-Laser Evaporation Technique for Deposition of Thin Films: Physics and Theoretical Model. *Phys. Rev. B* **1990**, *41*, 8843−8859.
(59) Shpak, A. P.; Korduban, A. M.; Medvedskij, M. M.; Kandyba, V. O. XPS studies of Active Elements Surface of Gas Sensors Based on WO_{3-x} Nanoparticles. *J. Electron Spectrosc. Relat. Phenom.* **2007**, *156*−*158*, 172−175.